

Charge correlations and transverse momenta observed in multifragmentation of 1 GeV/nucleon Au projectiles

G. Rusch, W. Heinrich, B. Wiegel,* E. Winkel, and J. Dreute
Fachbereich Physik, Universität-GH-Siegen, D-57068 Siegen, Germany
 (Received 26 March 1993; revised manuscript received 12 July 1993)

We have investigated the fragmentation of ^{197}Au projectiles at 0.85 to 1 GeV/nucleon in collisions with targets $(\text{CH}_2)_n$, C, and Pb. Using plastic nuclear track detectors all projectile fragments with charge $6 \leq Z_F \leq 77$ produced in a collision were observed in coincidence. The combination of C and $(\text{CH}_2)_n$ data allows us to extract the hydrogen component in measured distributions by the use of the statistical subtraction method. Our data show a target dependence of the multifragmentation process which indicates a nonequilibrated source of the fragments and/or the influence of the target nucleus on the relation between size and excitation energy of the spectator. In comparison to the prediction of the statistical model, the transverse momentum dispersions are enhanced with a dominant contribution by Coulomb repulsion between the fragments. Based on the sum of transverse momentum vectors of all fragments we conclude that multifragmentation is observed in collisions with a large momentum and energy transfer to the prefragment. Correlations in the azimuthal emission angles of the fragments are caused by mutual repulsion and momentum conservation. The idea that a liquid-gas phase transition of nuclear matter is the origin of multifragmentation is supported by our observations.

PACS number(s): 25.75.+r, 25.40.Sc, 25.70.Pq

I. INTRODUCTION

The reason why and how multiple fragments are formed in heavy-ion collisions is an open question. Is the process a prompt and cold breakup or are the fragments emitted by a hot, expanded, and equilibrated source? To evaluate the time scale of fragment formation, the coincident measurement of all produced nuclei is necessary. Fragment correlations indirectly include information about the process. The comparison of experimental results for different colliding systems at different energies and the confrontation of data with fragmentation model predictions is of particular interest.

Most of the models describing heavy-ion collisions favor a thermodynamical view of the scenario [1,2]. The size and excitation energy of the spectator determine the fragmentation channel in a statistical way. It is reasonable that the excitation energy increases with the number of primary nucleon-nucleon interactions at a constant relative velocity of the collision partners. Thus the fragmentation of the projectile spectator (the prefragment) depends in first order only on its size and not on the mass of the target nucleus. Data taken at the GSI ALADIN spectrometer support this view [3].

The inclusive yield of small fragments ($2 \leq Z_F \lesssim 20$) has been shown to follow a power law [4] which was the reason for the idea that multifragmentation is caused by a liquid-gas phase transition of nuclear matter. Hüfner has shown [5] that the power-law behavior is not neces-

sarily connected to a phase transition. However, a phase transition would additionally imply that the exponent τ of the power law becomes a minimum at the critical point and that the fragment yield far away from the critical region is described by an exponential function [6,7]. Both effects were observed in different experiments [8,9].

Plastic nuclear track detectors, particularly CR-39 which is the most sensitive one, are suitable to observe the heavy projectile residues ($Z_F \geq 6$) of peripheral and semicentral relativistic nucleus-nucleus collisions. We have used CR-39 in several experiments investigating fragmentation of nuclei up to charge $Z_P = 26$ (see [10] and references therein). In a first experiment [11] the technique has been applied to heavier projectiles for which multiple fragment production becomes important.

In continuation of this work on nucleus-nucleus collisions of heavy projectiles we have exposed different fixed target experiments to relativistic Kr, Ag, Au, and U beams with energies of 1.37, 1.45, 1.05, and 0.96 GeV/nucleon, respectively, at the Berkeley BEVALAC accelerator, to 1.0 GeV/nucleon Pb at the GSI SIS accelerator, and to 11.3 GeV/nucleon Au at the AGS in Brookhaven. Some important details of the experimental setup were improved to provide a completely computerized vertex reconstruction which reduces analysis time and enhances the statistics. In this paper we present results of the Au experiments at the BEVALAC.

II. EXPERIMENTAL METHOD

A. Detector setup and track measurement

Multifragmentation is not the dominant process in the observed sample of heavy-ion collisions because one deals

*Present address: Physikalisch-Technische Bundesanstalt, D-38116 Braunschweig, Germany.

with a random mixture of impact parameters having highest probability for peripheral collisions. Since our experimental technique has no trigger for any characteristic process, we mainly record noninteracting beam particles and spallation products. The statistics of multifragmentation events in our first experiment [11] suffered from this constraint. Furthermore, events in the energy range between 200 and 980 MeV/nucleon had to be combined. To overcome these disadvantages we used a different experimental setup with the aim to computerize the complete analysis from etch cone measurement to trajectory and vertex reconstruction.

Our new experimental setup concentrates on the reconstruction of events inside a homogeneous target at energies close to the beam energy. Instead of alternating target and detector layers [11] a thick target of about 2 g/cm² with detector foils assembled upstream and downstream is used (see Fig. 1). Gaps between adjacent detector foils reduce the influence of multiple scattering on the spatial resolution which is typically 3 μ m. This precision is essential for the automatic trajectory reconstruction of the incoming beam particles (up to 300 000) and their fragments. The sensitive detector area was enlarged to 12 cm \times 12 cm and the beam density was increased to about 2000 particles per cm². In the experiment described here, targets of (CH₂)_n, C, and Pb were exposed to the Au beam. By etching the detector foils for 24 h at 60 °C in 6*n* NaOH, etch cones visible through an optical microscope were developed. We measure the position and size of single etch cones on all detector foil sides using an automatic system as described in [12,13].

It was possible to enhance the statistics by a factor of 10 in comparison to Ref. [11]. We have analyzed 42 482 interactions Au+CH₂, 29 867 Au+C, and 8601 Au+Pb including all charge changing interactions with $\Delta Z \geq 2$. The contribution of multifragmentation depends on the target type. For Au+C we have best statistics with 2824 reactions having multiplicity three or more ($Z_F \geq 6$). Data from the C and CH₂ targets allow us to extract characteristics of the reaction Au+H by the statistical subtraction method.

B. Reconstruction of particle trajectories and vertices

The precision of mounting the foils in the experimental setup is a few hundred μ m but the statistical fluctuation of the particle's position is only a few μ m. Therefore precise spatial resolution is necessary for the reconstruction of all trajectories; those of the projectiles and of their fragments. For that purpose the individual foil coordinates must be transformed into a unique coordinate system. The spatial resolution which is obtained after completion of the reconstruction process contains a significant contribution from multiple scattering; the error caused by etch cone measurements is smaller than 2 μ m.

An essential tool for tracing the trajectories is the automatic recognition of a local track pattern. This guarantees the correct connection of etch cones on adjacent foil sides. Starting with beam particles on the frontside

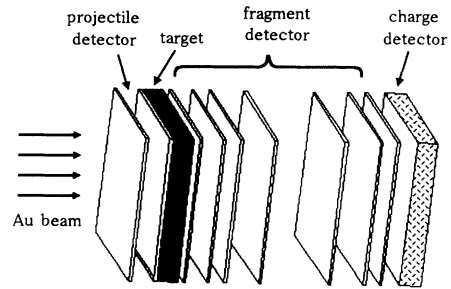


FIG. 1. Improved experimental setup consisting of a few CR-39 detector foils upstream and downstream of a thick target. A stack of foils at the end provides better charge resolution by multiple sampling.

of the first foil, their pattern is recognized on the backside and the coordinate transformation of this backside is evaluated. The assumption of exactly perpendicular incidence of all particles is implied in this procedure. In a subsequent step, when trajectories are traced over several foil sides, the direction of incidence is defined individually for each particle. This is important, e.g., for tracing through a thick target. Instead of the track pattern seen on the previous foil side one has to recognize the expected pattern based on individual directions of incidence. In general, both patterns are not equal to each other.

After reconstruction of beam particle tracks the unique coordinate system is defined. The next important point of track reconstruction is the search for additional sequences of etch cones lying on a straight line. The probability to find sequences of measured background objects is so small that no random track is expected to be found. On the other hand, the probability of reconstructing a real particle track is about 99%.

The first step of reconstruction is the exclusion of all noninteracting beam particles which are about 80% of all trajectories. For this purpose a preliminary charge calibration of the experiment is evaluated which assumes that the most frequent etch cone size measured on each detector foil side ("beam peak") originates from the projectiles. With this rough calibration the accuracy of the charge measurement for projectiles is $1e$ in front of and $0.5e$ behind the target. Based on this, all projectile candidates undergoing multifragmentation can be extracted unambiguously because a second fragment would only appear if the charge change ΔZ is greater than or equal to $\Delta Z = 6$.

After the identification of interacting projectiles the interaction vertices are reconstructed. For each fragment detected behind the target those incoming particles whose trajectories are closer than a distance d to the backward extrapolated fragment path are selected. Vertices with no secondary interaction of the fragments are reconstructed with a value of $d = 10 \mu$ m. This allows 90% of the interactions to be reconstructed unambiguously. The remaining 10% have a minimal distance of $d > 10 \mu$ m between the fragment and the best-fitting projectile trajectory, which may imply that there is more than one candidate for the vertex. Charge conservation or observation of a second fragment produced in one of

the possible vertices may help to decide between the alternatives in many cases. However, a small number of fragments (less than 3%) are connected to the wrong vertex. For this reason one must be careful with interpretation of rare process characteristics, in particular for the H data which have been calculated by subtracting the expected number of C data in the polyethylene target.

Vertices in the detector foils before and behind the target are excluded from further analysis using the reconstructed vertex depth and the sizes of the etch cones adjacent to the target as criteria. The precision of the reconstructed depth is about $200 \mu\text{m}$ depending on the scattering angle of the fragment. Interactions of incoming particles having lower charge than a beam projectile are not of interest for further analysis and are therefore excluded. Furthermore, vertices at the edge of the scan area must be excluded because they might be reconstructed incompletely due to escaping fragments.

C. Charge determination

The charge and energy of a particle must be assigned to each measured etch cone. This is done by a calculation of the energy loss in the layers between adjacent etch cones starting with the beam energy on the first foil side. For fragment tracks the initial energy per nucleon is set equal to that of the projectile at the interaction point. Therefore the vertices must have been reconstructed beforehand. According to the energy of the particle, the charge is calculated from the measured etch cone size by use of the calibration curve for the foil side. The calibration curve relates the cone size to the restricted energy loss (REL) which is a function of the charge and energy per nucleon [14]. The energy loss in a subsequent layer is calculated using the charge and energy assigned to the etch cone and a mass given by the EPAX code [15] (except for beam particles).

For the method of charge calculation described above a calibration is required. On the other hand, identification of the particle's charge is necessary for calibration. This problem is solved by an iterative process. Starting with calibration curves based on the beam peaks of each foil side, more and more charge peaks are extracted and then used to improve the calibration functions. For that purpose it is essential to determine charge averages over distances where no charge changing interaction takes place. The charge spectrum after the successful calibration of the experiment Au+CH₂ is shown in Fig. 2.

Since individual charges are not resolved for $Z_F \gtrsim 72$, charge peaks cannot be identified by counting charges downward beginning with the beam peak. However, the correct assignment for the lower charges in Fig. 2 can be verified with the help of fission interactions. The spectrum of the charge sum of events with multiplicity $M = 2$ rises toward charge 79 and then drops down rapidly. If the charge assignment is wrong by one charge unit, this drop would be shifted by two charge units. Thus our charge assignment is correct leading to a resolution σ of $0.15e$ at charge $Z_F = 6$, $0.35e$ at charge $Z_F = 26$, and $0.62e$ at charge $Z_F = 70$.

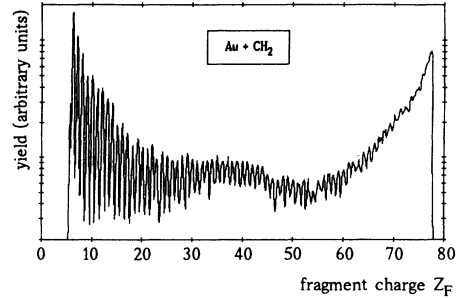


FIG. 2. Charge spectrum of all fragments detected in the experiment Au+CH₂. The lowest recorded charge is $Z_F = 6$, individual charges are resolved up to charge $Z_F = 72$.

Figure 3 shows the final calibration curves of all foil sides measured in the experiment Au+CH₂. The logarithm of the restricted energy loss (REL) is plotted against the quantity $1 - \beta^2$ which is 0 at the detector threshold and 1 at the maximum reachable etch cone size (β is the ratio between bulk and track etch rate). Two groups of calibration functions can be seen in Fig. 3, one including all graphs for the most sensitive CR-39 material "USF3," the other corresponding to "DOP" which is less sensitive but has less background objects on the surface after etching. From the detector threshold up to a value of $1 - \beta^2 = 0.9$ the USF3 calibration curve is approximately a linear function. This dependence is used to interpolate between the calibration points defined by the different charge peaks. The dispersion of the graphs inside each group reflects slightly different sensitivities, different conditions in the etching bath, and different conditions for track measurements on the foil sides due to varying illumination of the detector surfaces.

III. CHARGE PARTITION IN DIFFERENT FRAGMENTATION PROCESSES

An overview of the distribution of fragmentation processes is given in Fig. 4. For interactions (a) Au+H,

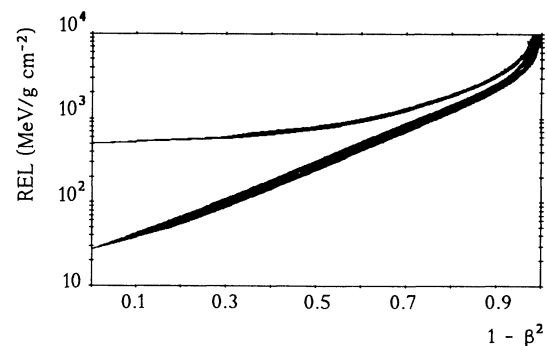


FIG. 3. Calibration functions of all detector foil sides mounted in the experiment Au+CH₂. The restricted energy loss, REL, is plotted against $1 - \beta^2$ with β the bulk etch rate divided by the track etch rate. The upper band corresponds to the less sensitive CR-39 of type "DOP," the lower band to "USF3."

(b) Au+C, and (c) Au+Pb the partition of the highest charge Z_1 and the sum of all lower charges $Z_2 \cdots Z_M$ (with $Z_F \geq 6$) is shown. The size of each box is proportional to the number n of events in this area [special symbols indicate numbers n above the maximum box content $n(\max)$]. In the bottom line all interactions with multiplicity $M = 1$ are included. Here spallation is dominant for all targets; a strong disassembly leaving just one small fragment occurs for targets C and Pb only, but

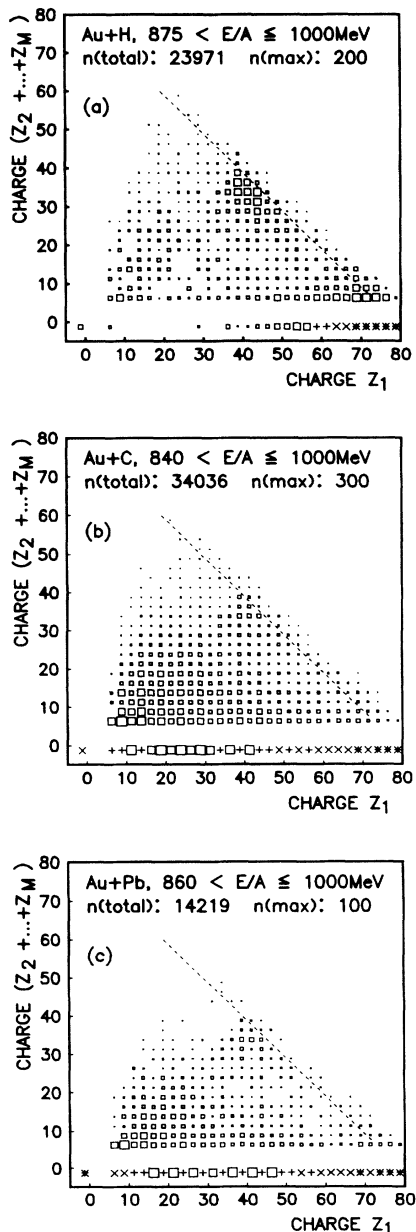


FIG. 4. (a)–(c): Charge correlations in interactions of Au+H, Au+C, and Au+Pb. The sum of all lower charges $Z_2 + \cdots + Z_M$ is plotted against the highest charge Z_1 . Box sizes are proportional to the number of events within the corresponding area (the content of the larger box is n_{\max}); special symbols indicate numbers above n_{\max} (+ for $n_{\max} \leq n \leq 2n_{\max}$, \times for $2n_{\max} \leq n \leq 5n_{\max}$, $*$ for $n \geq 5n_{\max}$).

not for proton-induced reactions. This observation is not surprising since the available energy in central collisions rises with target mass. For the same reason total disassembly (no fragment $Z_F \geq 6$), called vaporization, is most frequent for the Pb target and almost absent for the H target.

Multifragmentation resides on the left side of each plot of Fig. 4. For the H target only a few interactions of this type are observed. Due to the systematic uncertainties involved in the subtraction method between the C- and CH_2 -target results we do not claim that this rare process is observed in proton-induced reactions. Comparing multifragmentation in Figs. 4(b) and 4(c), the Pb data show a more pronounced concentration in the lower left-hand corner which means that high multiplicity events with several fragments ($Z_F \geq 6$) are less frequent in collisions of Au+Pb than in Au+C collisions.

Fission processes in the center of Figs. 4(a)–4(c) are more or less well separated from all other events. Symmetric binary decay is favored in fission without additional charge loss as well as in fission accompanied by proton evaporation. With almost the same yield a process called associated spallation, which has been previously observed [11], can be seen in the lower right-hand corner. Like fission, it is a binary decay but with one large and one small fragment formed. Contrary to fission, these events are not clearly separated from multifragmentation, which may indicate that these processes are not principally different. On the other hand, associated spallation is formally identical to the rare cluster decays observed for very heavy nuclei in the ground state [16]. If there is a link between both ends, a strong increase of this decay mode with excitation energy should be observed.

A few unrealistic events appear above the dashed line which indicates charge conservation. Since most of the intermediate mass fragments have low charges $Z_F = 6, 7, 8$ and most of the spallation fragments have high charges $Z_F = 77, 76, 75$, the combination of such fragments to a wrong vertex is statistically favored. The small number of events violating charge conservation confirms the good quality of vertex reconstruction.

One important fact displayed in Fig. 4 is that the populated branches of different fragmentation processes are widely spread. The remaining bound charge Z_B may be concentrated in one fragment as well as split into four small fragments ($Z_F \geq 6$). This can be seen in Fig. 4 by comparing event yields on lines parallel to the dashed line. The question is whether differences exist in the initial stages of those fragmentation channels or not. If not, the energy transfer into the spectator matter is subject to large fluctuations.

Interactions which produce 3 fragments of charge $Z_F \geq 6$ are typical multifragmentation events. Since the statistics for this class is quite good for the reaction Au+C, $M = 3$ interactions for this target are selected to analyze the charge partition and charge correlations in multifragmentation. Only experimental data will be shown. A comparison to model calculations is not within the scope of this paper. In the following the fragment charges are ordered by $Z_1 \geq Z_2 \geq Z_3$.

The partition of the available charge into the fragments is naturally restricted by charge conservation and therefore dependent on the distribution of Z_B (which is in average correlated to the impact parameter). For that reason the analysis of charge correlations including different values of Z_B is done in terms of the relative portions $\delta_1 = Z_1/(Z_1 + Z_2 + Z_3)$, $\delta_2 = Z_2/(Z_1 + Z_2 + Z_3)$, and $\delta_3 = Z_3/(Z_1 + Z_2 + Z_3)$. A purely random partition of Z_B can easily be computed by a Monte Carlo simulation. Taking into account that only integer numbers are valid and that fragments with charge lower than $Z_F = 6$ are not detected, we can compare this result with the measured distribution, being aware that all constraints are the same. In Fig. 5, δ_1 , δ_2 , and δ_3 are combined, the quantity δ and the ratio between measured and computed yield is shown. Small and high values of δ are most populated, whereas middle values are suppressed in the measured data. This indicates again that an asymmetric partition of the charge is preferred in multifragmentation.

The principal behavior shown in Fig. 5 does not change when the data are split into narrow intervals of Z_B , which means that an asymmetric partition is preferred for peripheral multifragmentation as well as for central collisions. However, only values of Z_B lower than 50 show the small peak around 0.38. This unexpected peak is caused by the value of the second highest charge Z_2 . It turns out that this charge tends to be equal to Z_1 or Z_3 , respectively. In Fig. 6 we present again the ratio between measured and computed yield, now for the quantity $(\delta_1 - \delta_2)/(\delta_1 - \delta_3)$ which is equal to $(Z_1 - Z_2)/(Z_1 - Z_3)$. The middle charge Z_2 obviously prefers to be equal to Z_1 or Z_3 and values around $\frac{1}{2}(Z_1 + Z_3)$ are slightly suppressed.

IV. TARGET DEPENDENCE OF FRAGMENT YIELDS

The charge sum Z_B of all projectile fragments is correlated with the impact parameter of the collision [17]. A more peripheral collision produces larger values of Z_B on average which means that Z_B can be taken as a scale for the centrality of the interaction. For that reason the Z_B dependence of the observables is of particular interest.

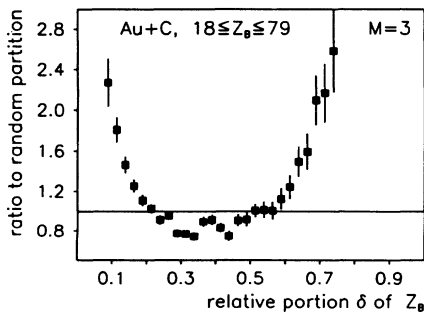


FIG. 5. Yield of charge portions $\delta_i = Z_i/(Z_1 + Z_2 + Z_3)$, $i = 1, 2, 3$, in Au+C events with multiplicity $M = 3$ compared to a random partition of the remaining bound charge $Z_B (= Z_1 + Z_2 + Z_3$ in this case).

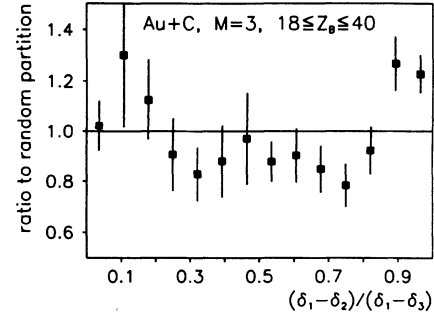


FIG. 6. Yield of the quantity $(\delta_1 - \delta_2)/(\delta_1 - \delta_3)$ with $\delta_i = Z_i/(Z_1 + Z_2 + Z_3)$, $i = 1, 2, 3$, in Au+C events with multiplicity $M = 3$ compared to a random partition of the remaining bound charge Z_B .

The ALADIN Collaboration has shown that for Au-projectile fragments the Z_B dependence of different observables is almost independent of the target [17]. This universal behavior suggests an equilibration of the fragment source prior to its decay, because no memory of the initial stage can be observed. Due to the different detector thresholds and beam energies our results cannot be compared directly to the ALADIN data. However, the observations can be compared qualitatively.

A. Multiplicity of intermediate mass fragments

Figure 7 shows the mean multiplicity $\langle M_{imf} \rangle$ of intermediate mass fragments ($6 \leq Z_F \leq 30$) as a function of Z_B measured for the interactions Au+H, Au+C, and Au+Pb. The data are not target independent, especially the proton-induced reactions are associated with higher multiplicities. A detailed analysis of the corresponding figure in Ref. [17] shows that data presented therein follow the same trend, the multiplicity rises with decreasing target size from Pb to C. For better comparison, the ALADIN data have been analyzed with our detection threshold of $Z_F \geq 6$ [18]. Although the difference between the C target and the Pb target turns out to be smaller in the ALADIN data, the two sets of $\langle M_{imf} \rangle$ data are not necessarily in contradiction since one must also account for the differences in beam energy.

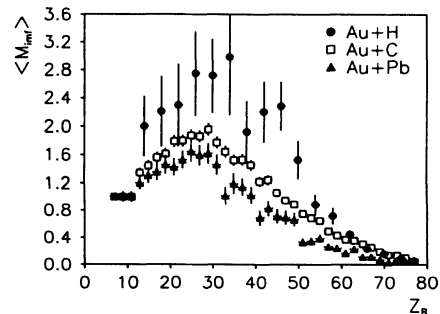


FIG. 7. Mean multiplicity of intermediate mass fragments ($6 \leq Z_F \leq 30$) in interactions of Au+H, Au+C, and Au+Pb plotted versus the remaining bound charge Z_B .

The mean multiplicities in proton-induced reactions exceed the C and Pb data significantly. Certainly multifragmentation in Au+H is a rare process which may cause experimental uncertainties by the subtraction of the C-target data from the CH₂-target data. However, the data points for $Z_B \geq 50$, which are less affected by statistical uncertainties, also show higher values of $\langle M_{\text{imf}} \rangle$ for Au+H in comparison to the other targets. The data for $Z_B < 50$ follow this trend. The information contained in Fig. 7 can be summarized by the statement that the multiplicity of intermediate mass fragments ($6 \leq Z_F \leq 30$) decreases with increasing target mass, for peripheral as well as for central collisions. This means that a certain amount of memory of the initial stage exists.

B. Inclusive mass yield of intermediate mass fragments

The idea that multifragmentation is caused by a liquid-gas phase transition of nuclear matter implies some consequences concerning the inclusive mass yield of lighter fragments. The functional behavior should follow a power law near the critical point and an exponential one far away from this point [6,7]. At the critical point the rise of the yield toward smaller fragments should reach a minimum. Thus the exponent τ of a fitted power law plotted as a function of Z_B should pass through a minimum when the critical temperature is exceeded in central collisions.

In Fig. 8 the exponents τ of the C- and Pb-target data show the expected behavior while for the H-target data no significant minimum can be observed. The exponents for the H target with $\tau \approx 3$ lie significantly above all other values. These observations can be well interpreted with the concept of a phase transition. Proton-induced reactions do not reach critical temperatures, they are always subcritical with high exponents τ . Collisions of Au+C and of Au+Pb cover a wider regime of excitations including temperatures above and below the critical temperature.

The fragmentation yields are not independent of the target nucleus, as shown in Sec. IV A. This seems to be in contradiction to the observations by the ALADIN

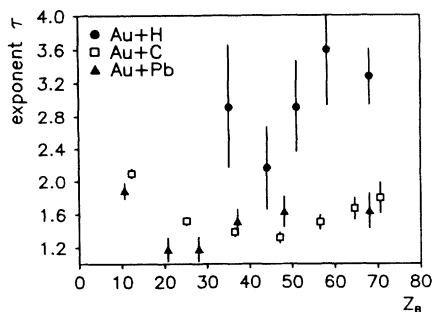


FIG. 8. Exponent τ of the power law fitted to the inclusive spectrum of light fragments ($6 \leq Z_F \leq 17$) in interactions of Au+H, Au+C, and Au+Pb plotted versus the remaining bound charge Z_B .

Collaboration [3,19]. However, the greatest difference appears for the H data which were not measured in Ref. [19]. Secondly, the exponent τ depends on the range of charges for which a power law was fitted. Extending this range to lower charges gives higher values of τ which means that data using different charge ranges for the fit cannot be compared directly. Last of all, the beam energy was not the same in both experiments. Another conclusion can be drawn from the fact that τ varies with the charge range where fitting is performed. Obviously the inclusive mass yield is not perfectly described by a power law. However, all our data are fitted significantly better by a power law than by an exponential function.

The rare multifragmentation events observed in the Au+H data again may be suspected to be artifacts (due to the subtraction of the C-target results from the CH₂-target results). The large contribution of small fragments to the total fragment yield (high τ values in Fig. 8) suggests that this is not the case. If proton-induced multifragmentation at this beam energy does not exist, the exponent τ should be almost equal to the value observed for C (mixed target CH₂). But the values derived for the Au+H results are higher in comparison to the other targets, for high Z_B (where the statistics are sufficient) as well as for lower values of Z_B . This supports the idea that a small amount of multifragmentation exists in collisions of Au+H at energies near 1 GeV/nucleon.

V. FRAGMENT TRANSVERSE MOMENTA

The distributions dN/dp_i of transverse momentum components p_i of fragments originating from light projectiles (C,O,Ar) are Gaussians [20,21]. These distributions result from momentum conservation of the nucleons in a sudden breakup of the projectile. Their standard deviations can be described based on the statistical model of Goldhaber [22] as $\sigma_{SM}^2 = \sigma_0^2 F(P-F)/(P-1)$, with mass numbers F and P of fragment and projectile and $\sigma_0^2 = p_F^2/5$ with Fermi momentum p_F of the nucleus. Additional contributions to the momentum dispersion are expected for heavier nuclei as a consequence of Coulomb interactions and possibly due to a bounce off in the collision. The final-state Coulomb interactions between the fragments have to be taken into account for the interpretation of the momenta observed in multifragmentation [23]. The results reported here show that Coulomb repulsion between the projectile fragments plays an important role for the final-state fragment momenta. However, multifragmentation is additionally correlated with a strong bounce off in the collision.

The distributions of the x and y components of transverse momenta analyzed in our experiment are identical within statistical accuracy. Therefore we combined both sets of data. The measured distributions of transverse momentum components are shown in Fig. 9 exemplary for some reactions. The distributions are well fitted by Gaussians except for the fission case [Fig. 9(f)]. So far, data agree with the expected form.

Our previous experiment [11] with lower statistics has shown that the transverse momenta of Au-projectile frag-

ments are enhanced in comparison to the values σ_{SM} expected from the statistical model. To calculate the transverse momentum from the emission angle of a fragment, we must fix two uncertain quantities, the longitudinal velocity $\beta_{||}$ and the mass A_F of the fragment. We assume that $\beta_{||}$ is equal to the value of the projectile at the interaction point. This assumption is valid with good accuracy for $\langle \beta_{||} \rangle$ (see [17]). However, the distribution of longitudinal momenta which cannot be taken into account on an event-by-event basis will cause a systematic broadening of our measured transverse momentum width. As described in [11] we have investigated this effect by a Monte Carlo simulation and found a broadening of only a few percent, which can be neglected.

The fragment mass A_F has to be estimated from the measured fragment charge. It was questioned by Morrissey [24] whether the charge to mass relation used in Ref. [11] is the origin of the observed momentum enhancement. The reanalysis of our data using the EPAX

mass formula [15] shows a slight decrease of the momentum dispersions but no general change of the observed momentum enhancement [25]. The data presented here are calculated using EPAX which has already been proven [26] to be accurate within $|\Delta A| \leq 1$.

Systematic errors mainly arise from secondary interactions of the fragments inside the target. We have chosen target thicknesses which guarantee that the probability of a secondary nuclear reaction is below 10%. The bias to the measured transverse momenta by multiple scattering inside the target is below 1% for light fragments and below 10% for heavy fragments in the case of the C and CH₂ targets. For the Pb target these values vary between 2% and 40%. We correct the momentum dispersion for this broadening by subtracting the calculated multiple scattering variance given in Ref. [27].

Data comparable to our results are available from target fragmentation experiments, in particular for proton-induced reactions. The systematics of the momentum

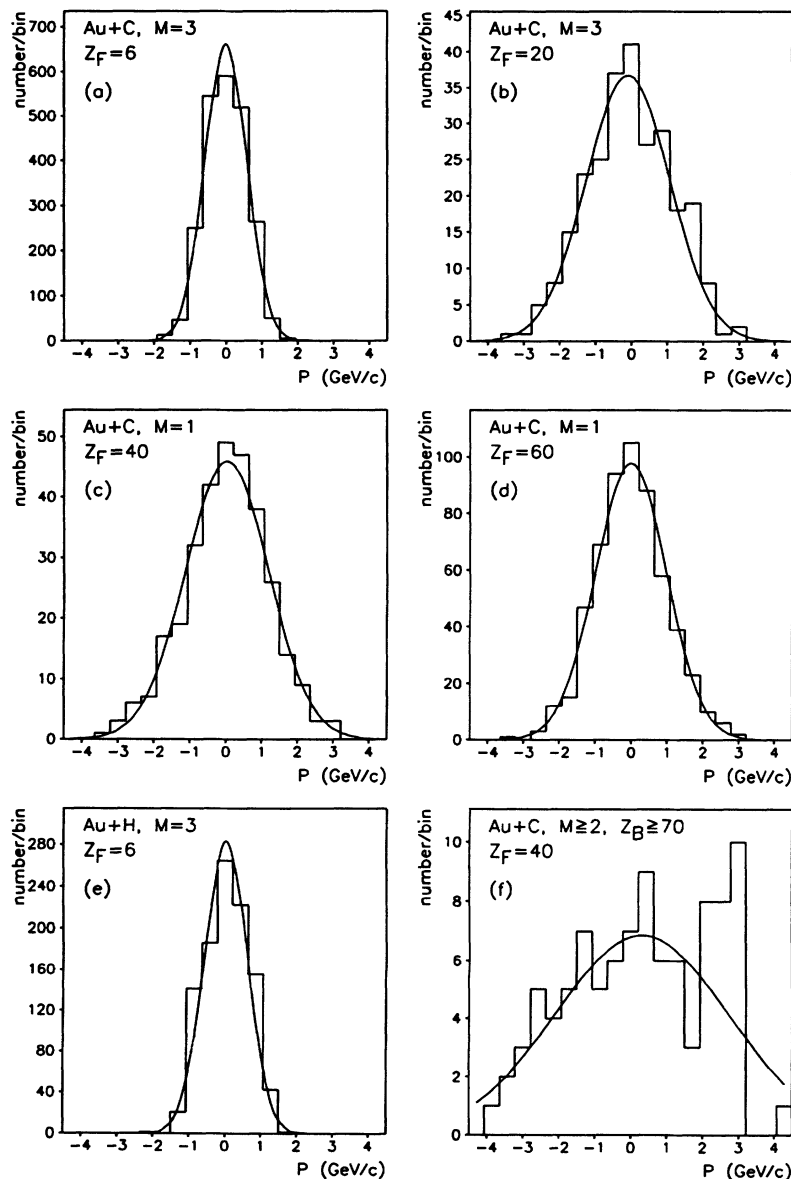


FIG. 9. Measured distributions of transverse momentum components for some reactions. The curves shown are fitted Gaussians.

distributions have been reviewed by Morrissey [28]. He has shown that fragment momenta of spallation products are well described by the statistical model even for heavy target nuclei. Our experiments with inverse kinematics give the same results for the spallation products of the reaction Au+H. This can be seen in Fig. 10(a) where the standard deviation σ of one transverse momentum component is plotted against the mass A_F of the fragment. The data shown in Fig. 10 are restricted to conditions which include only data points with dominant contributions from spallation or multifragmentation events, respectively. Especially $M = 1$ events were ex-

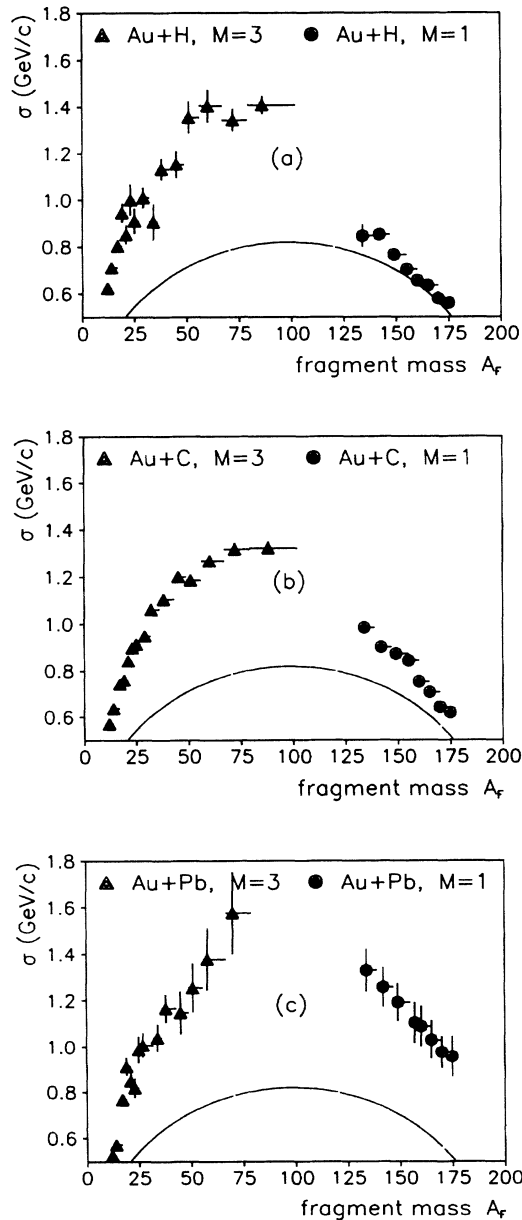


FIG. 10. Transverse momentum dispersion σ of multifragmentation ($M = 3$) and spallation reactions ($M = 1$ and $A_F \geq 120$) for (a) Au+H, (b) Au+C, and (c) Au+Pb compared to the statistical model (solid line). The horizontal bars on the data points show the bandwidth for A_F .

cluded for $A_F < 120$. The σ values of heavy remnants almost agree with the prediction of the Goldhaber formula, using $p_F = 260$ MeV/c [29] which is drawn as a solid line. On the other hand, transverse momenta of the smaller fragments produced by multifragmentation are significantly enhanced. For fragments of Au with large mass losses produced in proton-induced target fragmentation experiments [28] this enhancement of the momentum widths in comparison to predictions of the statistical model has been previously observed. Our results for different targets allow us to study these deviations from the statistical model in more detail.

The comparison of results for the different targets H, C, and Pb in Figs. 10(a)–10(c) shows no significant target dependence of the transverse momenta in the multifragmentation regime. For spallation processes ($A_F \geq 120$) the transverse momenta increase with target mass which may be explained by Coulomb repulsion between the projectile, or projectile remnant, and the target nucleus. An additional contribution may arise from dynamical collision momentum transfer as has been discussed recently [30]. It is important to recognize that a Coulomb contribution only appears in the transverse momenta and not in the longitudinal component which is measured in the target fragmentation experiments discussed in [28].

The coincidence measurement of all fragments with $Z_F \geq 6$ allows us to separate results for different interaction characteristics. This is done in Fig. 11 for the reaction Au+C where we have the best statistics. Instead of the absolute width σ we present here the ratio σ/σ_{SM} as a function of the fragment mass A_F . Results for events with multiplicity $M = 1$ are drawn as circles. The events with higher multiplicity are split into two groups which are distinguished by the charge sum Z_B of all observed fragments ($Z_F \geq 6$). This remaining bound charge is assumed to be correlated on average with the impact parameter of the collision (see Ref. [31]). Thus the solid triangles in Fig. 11 include the most peripheral interactions with binary decay (fission and associated spallation). The open triangles in Fig. 11 include those fragments which are produced in multifragmentation reactions.

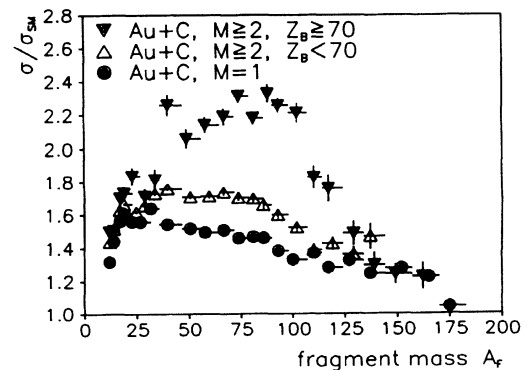


FIG. 11. Ratio σ/σ_{SM} of measured and predicted transverse momentum dispersion for three different types of Au+C reactions, single fragment production ($M = 1$), multifragmentation ($M \geq 2, Z_B < 70$), and fission ($M \geq 2, Z_B \geq 70$).

It can be seen in Fig. 11 that the transverse momentum dispersions of the fragments vary with the underlying fragmentation process. In comparison to events with higher multiplicity, the $M = 1$ events have the lowest transverse momenta. But even they show an enhancement compared to the statistical model, which increases with the centrality of the reaction, i.e., with decreasing A_F . A comparison of the momentum dispersions for different fragmentation processes at the same values of A_F shows that the transverse momenta decrease with the centrality of the collision, i.e., from $Z_B \geq 70$, $M \geq 2$ to $M = 1$. In the case of fission and probably also associated spallation, Coulomb repulsion between the two fragments is dominant whereas any statistical contribution to the transverse momenta can be neglected. This idea can be verified by a comparison of the measured transverse momentum dispersion with that calculated by the potential of a tangent sphere geometry (see Ref. [32]) and isotropic emission. The measured values amount to 80–90% of the calculation which is good agreement for such an idealized model.

The transverse momenta of the fragments observed in multifragmentation events are a combination of momentum transfer during the collision (statistical origin and bounce off) and mutual repulsion after freeze out of the individual fragments. The second contribution dominates for low ratios Z_F/Z_B because in this case the scattering angle of the prefragment is small in comparison to that of the final fragments. This explains the target independence for multiplicity $M = 3$ seen in Fig. 10.

To get an impression of the momentum transfer during the collision in multifragmentation events we have summed up the transverse momentum of $M = 3$ events. In Fig. 12 the standard deviations of the transverse momentum components for this sum (reaction Au+C, solid triangles) are shown. They are plotted against the EPAX mass calculated from the charge sum of the fragments. For comparison, the standard deviations for single fragments ($M = 1$) are plotted as open circles. The data show significant differences for prefragments of the same mass between multifragmentation events and spallation events. The momentum transfer is larger in the case

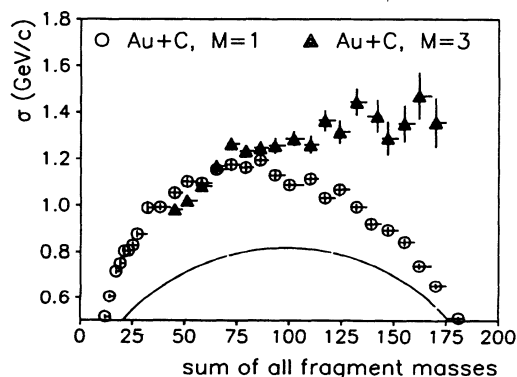


FIG. 12. Dispersion σ of the transverse momenta vector sum of all fragments in multifragmentation ($M = 3$, solid triangles) and spallation reactions ($M = 1$, open circles) for the reaction Au+C.

of multifragmentation. We conclude that strong fluctuations exist. The transverse momenta of prefragments, under certain conditions, can exceed the values expected from statistical effects and mutual Coulomb effects between projectile (prefragment) and target nucleus. Those events with high momentum (and probably also energy) transfer can undergo multifragmentation or, if they lose their excitation energy by emission of a larger number of light particles, end at sufficiently smaller masses and momenta and contribute to the $M = 1$ events in Fig. 12, or completely disintegrate.

VI. AZIMUTHAL CORRELATIONS

Our measurements allow us to study fragment correlations on an event-by-event basis. The nonisotropic emission of fragments already found in Ref. [33] can be analyzed in more detail based on the data of this experiment. Two different effects may influence the azimuthal emission angles of all fragments. First, small relative momenta between the fragments would be suppressed if the fragments are emitted almost simultaneously. As a consequence small azimuthal angles would be suppressed also. Second, the constraint of total momentum conservation (including the unobserved target fragments and nuclei with charge $Z_F < 6$) may favor a back-to-back emission. Both effects are observed unambiguously in the Au+C reaction data.

To investigate the influence of momentum conservation we have performed a Monte Carlo simulation. This simulation is based on a two-step model which assumes the existence of a prefragment. Kinematic properties of the prefragment are determined by the measured sum S_{PT} of the transverse momenta of all fragments observed. In the coordinate system of the prefragment, the momenta of the final-state fragments are simulated with Gaussian distributions which satisfy the constraint of momentum conservation. The charge dependent width is taken from the measured values shown in Fig. 10. Finally, these momenta are projected onto the plane perpendicular to the projectile directions.

The global structure of the azimuthal correlations observed can be explained by momentum conservation. This can be seen in Fig. 13(a) where the yield of emission angles of the two lighter fragments relative to the heaviest fragment is displayed for Au+C collisions with multiplicity $M = 3$. Isotropic emission would correspond to a constant value of 1. The emission of fragments in a direction opposite to the heaviest fragment is favored. This is clearly reproduced by the Monte Carlo simulation taking into account momentum conservation. The Pb data in Fig. 13(b) suffer from low statistics. Nevertheless they differ significantly from carbon-induced reactions; not only the data but also the simulation. The reason is that the dispersion of the scattering angle of the prefragment is greater in the case of the Pb target. This is shown in Fig. 14 where the distribution of the sum S_{PT} is displayed. The increased capacity of the large number of unobserved particles to carry momentum widens the phase space and reduces the correlations between the particles measured.

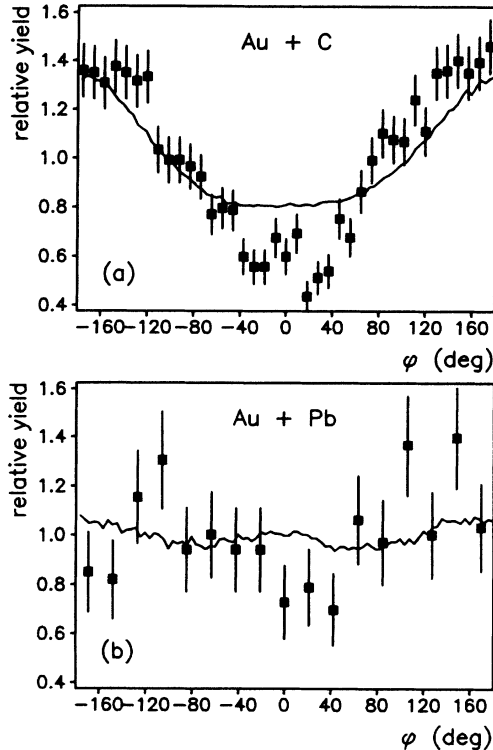


FIG. 13. Yield of the azimuthal emission angle φ of the lighter fragments relative to the heaviest fragment measured in interactions with multiplicity $M = 3$: (a) C target, (b) Pb target. The results of a Monte Carlo simulation is shown as a solid line.

The remaining discrepancy in Fig. 13(a) between data and simulation for the Au+C system at small angles reflects the influence of mutual Coulomb repulsion. We must leave open the question whether a typical emission time can be associated with the data. This would necessitate model calculations with defined freeze-out configurations. However, it is evident that correlations between azimuthal emission angles of multifragments, on the one hand, reflect total momentum conservation, and, on the other hand, show an additional contribution due

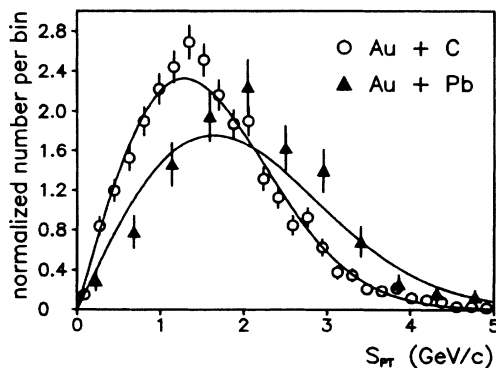


FIG. 14. Distribution of the vector sum S_{PT} of the observed transverse fragment momenta in reactions Au+C and Au+Pb with multiplicity $M = 3$.

to final-state Coulomb interactions. Thus the fragment formation time is so short that the process cannot be described sequentially.

VII. CONCLUSION

Charge correlations do exist between the fragments formed in multifragmentation processes. The charge partition tends to be more asymmetric than a pure random distribution. Thermodynamical and percolation models which calculate exclusive fragment yields of multifragmentation should reproduce these data. This reduces the parameter space of the models. The weak systematics shown in Fig. 6 for the size of the second heaviest fragment in more central collisions may give new information about the decay. One idea to explain these correlations is the subfission of fragments which would form two fragments of approximately the same size. But this is in contradiction to the fact that no subfission of the fission products themselves has been observed (this is not shown here explicitly, but in [33]). The correlations shown in Fig. 6 are not yet understood.

The target and Z_B dependence of the exponent τ shown in Fig. 8 support the idea that multifragmentation is caused by a liquid-gas phase transition. This result may be confirmed in the future by data taken at higher beam energies. Since the excitation energy rises with the energy of the projectiles, the exponent τ in reactions of Au+H should decrease with increasing energy and should pass through a minimum. Proton-induced target fragmentation data show that the energy transfer saturates at energies around 10 GeV [32]. Therefore data taken at the AGS in Brookhaven should clarify this. For collisions with heavier targets we expect a shift of the τ minimum to higher values of Z_B with increasing energy. The analysis of these data is in progress.

The mean multiplicity at constant values of Z_B falls with increasing target mass. This observation need not rule out an equilibrated source of fragments because differences may exist in the relation of the spectator size to the excitation energy. In the geometrical picture, interactions with a heavier partner but equal Z_B correspond to more peripheral collisions. Thus heating of the spectator matter takes place in peripheral areas whereas a small reaction partner deposits its energy deeper inside the spectator. In the first case a large amount of excitation energy may be lost during equilibration by particle emission from the hot border region, in the second case less energy can escape. An important question in this context is the magnitude of fluctuations in excitation energy at constant impact parameter. The data for the transverse momenta of the fragments indicate that these fluctuations are large. Multifragmentation occurs when the transfer of momentum (and energy) is large.

With our experimental technique we are also able to measure multifragmentation of heavy projectile nuclei at ultrarelativistic energies. From experiments at 11.3 GeV/nucleon we will hopefully obtain information about the saturation of energy deposition and the supercritical region of multifragmentation.

ACKNOWLEDGMENTS

The authors thank H. J. Crawford, J. Engelage, and all other members of the BEVALAC operations staff for

their excellent support. We thank P. Kreutz from GSI for providing us with multiplicity data of the ALADIN with respect to our experimental cuts. This work has been funded by the Bundesminister für Forschung und Technologie (BMFT) under Contract No. 06 SI 356.

-
- [1] W. A. Friedman, *Phys. Rev. C* **42**, 667 (1990).
 [2] D. H. Gross, *Rep. Prog. Phys.* **53**, 605 (1990).
 [3] C. A. Ogilvie *et al.*, *Phys. Rev. Lett.* **67**, 1214 (1991).
 [4] R. W. Minich, S. Agarwal, A. Bujak, J. Chuang, J. E. Finn, L. J. Gutay, A. S. Hirsch, N. T. Porile, R. P. Scharenberg, and B. C. Stringfellow, *Phys. Lett.* **118B**, 458 (1982).
 [5] J. Hüfner and D. Mukhopadhyay, *Phys. Lett.* **173B**, 373 (1986).
 [6] M. E. Fisher, *Physics (N.Y.)* **3**, 255 (1967).
 [7] A. D. Panagiotou, M. W. Curtin, and D. K. Scott, *Phys. Rev. C* **31**, 55 (1985).
 [8] A. S. Hirsch, A. Bujak, J. E. Finn, L. J. Gutay, R. W. Minich, N. T. Porile, R. P. Scharenberg, B. C. Stringfellow, and F. Turkot, *Phys. Rev. C* **29**, 508 (1984).
 [9] B. Berthier, R. Boisgard, J. Julien, J. M. Hisleur, R. Lucas, C. Mazur, C. Ngô, and M. Ribrag, *Phys. Lett. B* **193**, 417 (1987).
 [10] S. E. Hirzebruch, W. Heinrich, K. D. Tolstov, A. D. Kovalenko, and E. V. Benton, *Phys. Rev. C* **46**, 1487 (1992).
 [11] J. Dreute, W. Heinrich, G. Rusch, and B. Wiegel, *Phys. Rev. C* **44**, 1057 (1991).
 [12] W. Trakowski, B. Schöfer, J. Dreute, S. Sonntag, C. Brechtmann, J. Beer, H. Drechsel, and W. Heinrich, *Nucl. Instrum. Methods* **225**, 92 (1984).
 [13] G. Rusch, E. Winkel, A. Noll, and W. Heinrich, *Nucl. Tracks Radiat. Meas.* **19**, 261 (1991).
 [14] E. V. Benton, Report No. Tech. Rep. 68-14, USNRDL, 1968 (unpublished).
 [15] K. Suemmerer, W. Bröchle, D. J. Morrissey, M. Schädel, B. Szweryn, and Y. Weifan, *Phys. Rev. C* **42**, 2546 (1990).
 [16] P. B. Price, *Nucl. Phys.* **A502**, 41C (1989).
 [17] J. Hubele *et al.*, *Phys. Rev. C* **46**, 1577 (1992).
 [18] P. Kreutz (private communication).
 [19] P. Kreutz, Report No. GSI-92-23, 1992 (unpublished).
 [20] D. E. Greiner, P. J. Lindstrom, H. H. Heckman, B. Cork, and F. S. Bieser, *Phys. Rev. Lett.* **35**, 152 (1975).
 [21] Y. P. Viyogi *et al.*, *Phys. Rev. Lett.* **42**, 33 (1979).
 [22] A. S. Goldhaber, *Phys. Lett.* **53B**, 306 (1974).
 [23] Y. D. Kim, R. T. de Souza, C. K. Gelbke, and W. G. Gong, *Phys. Rev. C* **45**, 387 (1992).
 [24] D. J. Morrissey, *Phys. Rev. C* **47**, 413 (1993).
 [25] J. Dreute, W. Heinrich, G. Rusch, and B. Wiegel, *Phys. Rev. C* **47**, 415 (1993).
 [26] J. Pochodzalla (private communication). Recent results of the ALADIN Collaboration.
 [27] J. D. Jackson, *Classical Electrodynamics* (Wiley, New York, 1975), p. 777.
 [28] D. J. Morrissey, *Phys. Rev. C* **39**, 460 (1989).
 [29] E. J. Moniz, I. Sick, R. R. Whitney, J. R. Ficenece, R. D. Kephart, and W. P. Trower, *Phys. Rev. Lett.* **26**, 445 (1971).
 [30] F. Khan and L. W. Townsend, *Phys. Rev. C* **48**, R513 (1993).
 [31] J. Hubele *et al.*, *Z. Phys. A* **340**, 263 (1991).
 [32] J. Hüfner, *Phys. Rep.* **125**, 129 (1985).
 [33] C. Lewenkopf, J. Dreute, A. Abdul-Magd, J. Aichelin, W. Heinrich, J. Hüfner, G. Rusch, and B. Wiegel, *Phys. Rev. C* **44**, 1065 (1991).